Eur. Phys. J. Special Topics **229**, 145–155 (2020)

https://doi.org/10.1140/epjst/e2019-900111-5

THE EUROPEAN PHYSICAL JOURNAL SPECIAL TOPICS

Regular Article

Experimental and simulation studies of solidification behaviour in undercooled CuCoNi equiatomic medium entropy alloy

M.R. Rahul and Gandham Phanikumar[a]

Department of Metallurgical and Materials Engineering, Indian Institute of Technology Madras, Chennai 600036, India

Received 17 June 2019
Published online 11 February 2020

Abstract. Undercooling studies were carried out in equiatomic CuCoNi system with an aim to understand the growth kinetics and microstructural variations as a function of undercooling. The morphological change in microstructure was observed and correlated with the undercooling obtained. Non-linear variation of growth velocity with respect to the increase in undercooling was obtained from high-speed video measurements. The variation in growth velocity was compared with the dendritic growth model with a modified kinetic undercooling term. The segregation profile was predicted using multi-phase field method and compared with the experimental data. Micro-hardness variation was correlated with the undercooling obtained.

1 Introduction

Development of high entropy alloys leads to the design and exploration of other equiatomic and medium entropy alloys [1,2]. The medium entropy alloys with remarkable properties gained attention in recent time [3]. Solidification studies on ternary equiatomic alloys will pave an easier path to understanding microstructure evolution in multi-component high entropy alloys. The equiatomic alloys like CoCrNi [4–6] are studied in literature mainly focused on structural property correlation with the microstructure. HEA shows remarkable properties that are not readily explained by characteristics of the constituent elements [1,7]. The systematic study of HEA and its derivatives are required to properly optimise the material design domain as well as to attain property enhancement through material processing. The reported equiatomic multi-principle element based alloys are processed by different routes like mechanical alloying and sintering, conventional casting, vacuum arc melting, induction melting, etc [8]. The advent of the newly emerging field like additive manufacturing demands the study of material in extreme or non-equilibrium conditions [9–11]. An understanding of solidification microstructure evolution as function of undercooling will help in relating the processing conditions of different melt based techniques with the final microstructure and properties.

The studies on high entropy alloy systems such as FeCoNiCrCu [12–14], AlFeCoNiCu [15], FeCoNiCuMn [16], etc. show the microstructural variation in as

[a] e-mail: gphani@iitm.ac.in

cast as well as thermo-mechanical processing condition. The phase separation was observed in HEAs with transition metals [11] and FeCoNiCuNb system shows that liquid phase separation was accelerated with an increase in Nb concentration [17]. The FeCoCuCrNi system shows liquid phase separation in undercooled condition after attaining a critical undercooling and the corresponding growth velocity data show the velocity was less compared to Ni-based alloys [14,18]. From these systems, the binary derivatives such as Co–Cu system will show liquid phase separation even in lower undercooling regime [19] and Ni–Cu system will not undergo any liquid phase separation during undercooling studies so far reported [20]. From these studies in HEAs the microstructure modification depends on the processing condition as well as constituent elements [1,21]. The undercooling studies can be carried out to access the behaviour of the material at extreme non-equilibrium processing condition. The undercooling studies on Cu–Ni system show morphological changes in the microstructure with respect to undercooling obtained [20,22]. Undercooling studies on CoCuNi system was reported in literature mainly concentrated on the Co or Cu rich region and shows liquid phase separation in deep undercooling [23]. The studies on the equiatomic system were not yet explored.

In this study, one of the derivatives of the HEA namely the equiatomic CoCuNi system was selected for the undercooling study using melt fluxing technique. The growth velocity was established using high-speed video analysis and correlated with the dendritic growth model. The segregation profile of undercooled sample was predicted using phase-field modelling. The mechanical property of undercooled sample was evaluated using microhardness measurements.

2 Experimental details

The alloy of the required composition was prepared by using a vacuum arc melting process. The pure elements (99.9%) of required composition in atomic percentage was taken and melted in the chamber using an arc stuck between a non-consumable Tungsten electrode and the Cu hearth. The chamber is first evacuated to a vacuum pressure of 2×10^{-5} mbar and backfilled with high purity Argon gas to get the arc. The sample is flipped each time before melting and its homogeneity was ensured by melting the sample for five times. The prepared alloy was cut into required weights using an electrical discharge machining process. The undercooling experiment was carried out using melt fluxing technique, the sample is placed in a quartz tube with boron trioxide flux and experiment was carried out in an Argon atmosphere. The temperature from the sample was captured by using a non-contact infrared pyrometer and monitored using Infrawin® software. The high-speed video was captured during the recalescence time using a high-speed video camera of Photron® made with the frame rate of 100 000 per second. The captured video was analysed by using PFV® software and growth velocity was established.

The as-cast sample and undercooled sample was polished by standard metallographic polishing technique. The polished sample was analysed using scanning electron microscopy in backscattered electron mode (Quanta 400®-FEI® made) and the compositional analysis was carried out by energy disperse spectroscopy (EDS) using Bruker® detector. The structural characterisation of the as-cast and the undercooled sample was carried out using XRD with a step size of 0.0167. The microhardness was performed using a load of 500 gf with a dwell time of 10 s.

Table 1. Parameters used for phase field simulation.

Parameter	Value and unit
Diffusion constant of Co in the melt	$6.01 \times 10^{-6}\,cm^2/sec$
Diffusion constant of Co in the dendrite	$6.01 \times 10^{-10}\,cm^2/sec$
Diffusion constant of Cu in the melt	$2.46 \times 10^{-5}\,cm^2/sec$
Diffusion constant of Cu in the dendrite	$2.46 \times 10^{-10}\,cm^2/sec$
Kinetic coefficient (μ) between phases liquid and primary dendritic phase [$cm^4/(Js)$]	65.00000×10^{-4}
Surface energy between phases liquid and primary dendritic phase [J/cm^2]	1.00000×10^{-5}
Domain size, Grid size	$200 \times 200\,\mu m$, $0.1\,\mu m$

3 Simulation details

Phase-field simulation was carried out using commercial microstructure simulation software Micress®. The simulation was carried out to predict the segregation behaviour of elements during the solidification of the primary FCC phase. The real-time coupling with the thermodynamic database Thermo-Calc® was established by using TQ interface between Thermo-Calc® database and Micress®. The diffusion data required for the simulation were optimised while considering the order of magnitude for normal dilute alloys. The optimised values for mobility and surface energy data were shown in Table 1. The thermodynamic data were taken from TCHEA2 database. The phase field and diffusion equation were solved and the plots are obtained. The equation solved for the solidification process was explained elsewhere [24–26]. The obtained plots are compared with the segregation profiles from the experimental compositional analysis. The virtual line EDS was generated in the simulated sample and compared with the experimental line EDS. In order to determine the effect of undercooling the undercooling temperature was changed keeping all other parameters constant and the phase map was plotted with a constant time step. A realistic microstructure simulation was carried out using multiple dendrites and compared with the experimental EDS mapping results.

4 Results and discussion

4.1 As-cast microstructure

The as-cast microstructure is shown in Figure 1. The phase formation was predicted by Thermo-Calc® using TCHEA2 database, Scheil's solidification simulation (Fig. 1a) shows the formation of phase with FCC structure. The Thermo-Calc® predicts a liquidus temperature of 1672 K and the undercooling thermal cycle shows a liquidus temperature more than 1672 K. Further calculation of undercooling was carried out using 1672 K as liquidus temperature. The as-cast BSE-SEM image shown in Figure 1b consists of the primary dendritic region, interdendritic region and grey colour minor region. The EDS mapping (Fig. 1c) confirms that the primary dendritic region was rich in Co-Ni and the interdendritic region was enriched with Cu, the minor phase was enriched with Co. The structure of the major Co–Ni region is shown in XRD pattern (Fig. 1d) where the Cu having close lattice parameter with Co-Ni rich phase causes the overlap and the minor phase was outside the detectable range of the current XRD measurements. The XRD pattern confirms that the Thermo-Calc® prediction was valid for the current system.

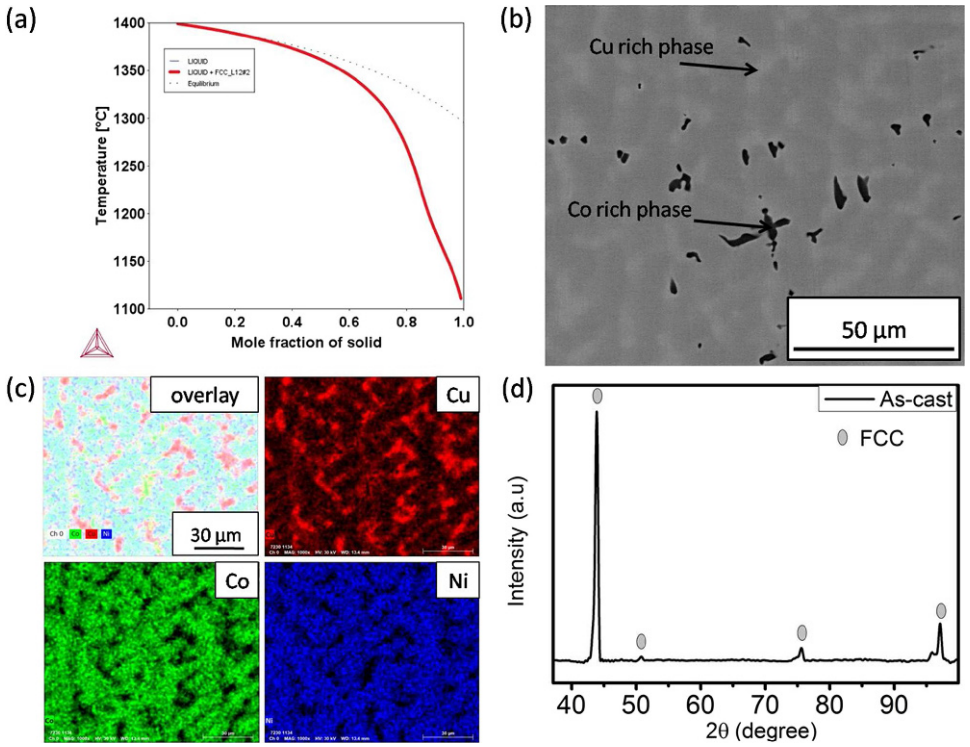

Fig. 1. Thermodynamic prediction and characterisation of as-cast sample (a) Scheil's solidification plot shows formation of FCC single phase, (b) SEM- BSE image shows formation of primary Co-Ni rich phase, Cu rich interdendritic region and Co rich minor phase, (c) EDS mapping shows segregation of Cu at the interdendritic region and uniform distribution of Ni and Co in the dendritic region, (d) XRD pattern shows the major phase has FCC structure.

4.2 Thermal cycle characteristics and high-speed video imaging

The temperature vs. time data were collected at each experiment to establish the undercooling obtained. Figure 2 shows the typical thermal cycle collected during an undercooling experiment ($\Delta T = 57\,\mathrm{K}$). The heating part shows the slope change at the liquidus temperature and the sample was superheated ~200 K above the liquidus temperature. The superheated sample was cooled as shown in the cooling part, the recalescence was observed during the primary phase solidification. The inset shows the recalescence event happens due to the release of latent heat during solidification. The recalescence event, in turn, causes a distinct liquid-solid interface due to the high temperature of solid because of latent heat coming out. This was captured using high-speed video imaging (shown as snapshots) and the solid-liquid interface was tracked to get the growth velocity variation with respect to undercooling obtained. The undercooling was measured as the difference between liquidus temperature (T_L) and nucleation temperature (T_N). A maximum undercooling of around 150 K was obtained in this system.

4.3 Microstructure evolution during undercooling

The microstructural variation with respect to undercooling obtained is shown in Figure 3. Cu has miscibility with Ni at a higher temperature and is immiscible with

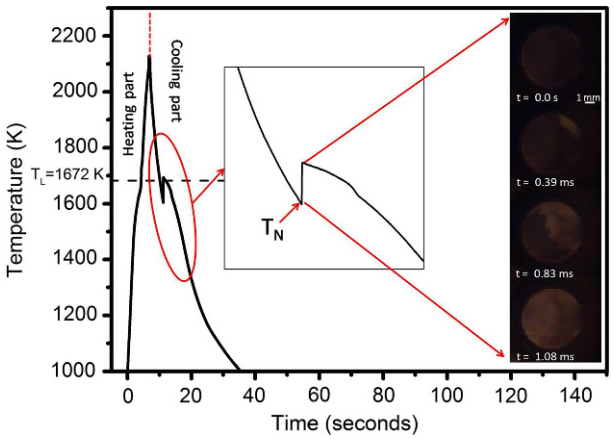

Fig. 2. Complete thermal cycle for undercooling experiment ($\Delta T = 57\,\mathrm{K}$), inset shows the recalescence event during solidification where T_N represents the nucleation temperature. Corresponding high speed snapshots collected are shown.

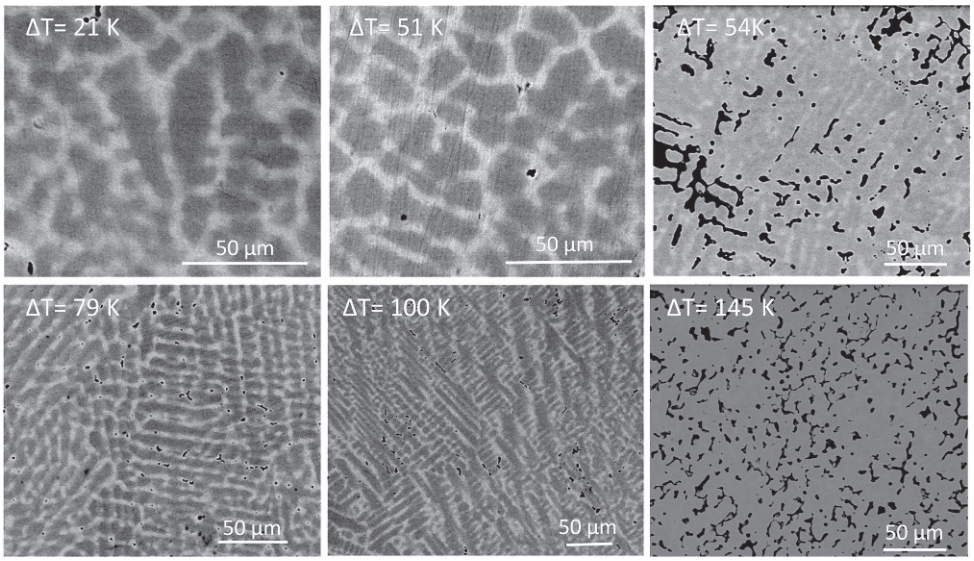

Fig. 3. SEM-BSE images of undercooled samples at different levels of undercooling show the variation of morphology with undercooling achieved.

Co makes the equiatomic system more relevant to study the microstructure evolution. The microstructure evolution shows no liquid phase separation even an undercooling of above 150 K. Since Cu has positive enthalpy of mixing with Co (6 kJ/mol) it will segregate out from the Co-rich primary phase, Ni has lower enthalpy of mixing with Co (0 kJ/mol) and is likely to lead to formation of Co–Ni rich phase [27]. The morphological variation with respect to undercooling in binary Cu–Ni system was dominated by dendrite remelting at lower undercooling regime and recrystallization at higher undercooling regime [28].

The microstructure shows morphological changes from lower to higher undercooling regimes. Up to 21 K, the microstructure is coarse dendritic with Cu rich interdendritic region. In the undercooling range $21 < \Delta T < 54\,\mathrm{K}$, the microstructure consists of partial dendritic and grain structure. This microstructure consisting of

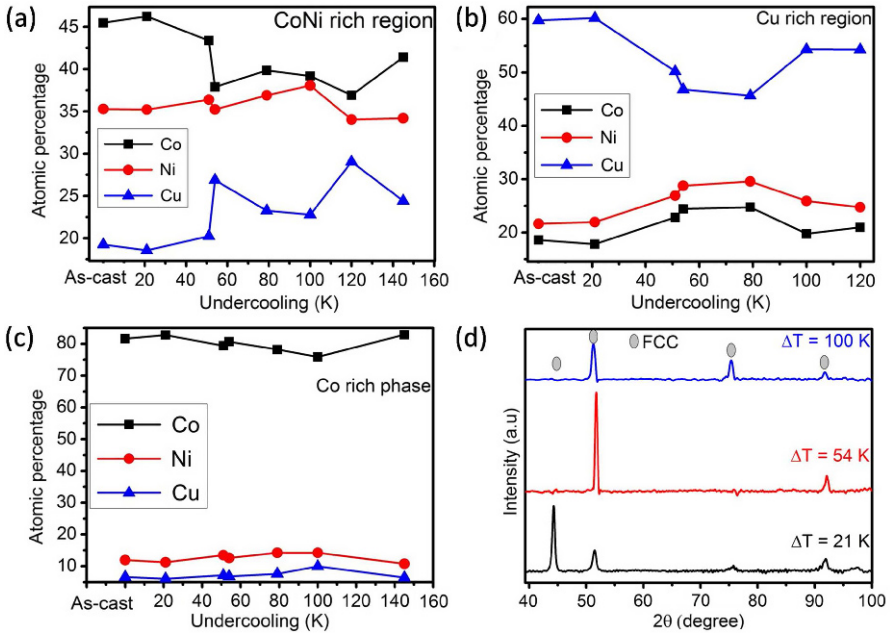

Fig. 4. Plot shows the EDS compositional analysis at different phases (a) Co–Ni rich phase, (b) Cu rich interdendritic region, (c) Co rich region and (d) XRD pattern at different level of undercooling.

Cu segregation around the dendrites can be attributed to the dendrite remelting and leading to the solidification of Cu rich region on the surrounding regions. In the case of 54 K $< \Delta T <$ 100 K the microstructure consists of partial grain and columnar dendrite morphology. Above 100 K the microstructure shows distorted dendritic or fine dendritic morphology with shrinkage defects. The shrinkage defects may be due to the distortion of dendrite due to volume change during solidification or by dendrite remelting. The Cu rich interdendritic region was absent in the interdendritic region.

Figure 4 shows the EDS analysis of individual phases, in the Co–Ni rich phase, the EDS profile (Fig. 4a) shows that the amount of Co get depleted in the primary dendritic phase with increase in undercooling and Cu amount get increased with respect to undercooling. The increase in Cu in the primary dendritic phase was attributed to the solute trapping effect and which can also be confirmed by the increase in growth velocity in the higher undercooling regime. The Ni concentration in Co–Ni rich phase remained almost the same with respect to increasing undercooling. The concentration of elements in the interdendritic region is shown in Figure 4b, it confirms that the Cu concentration was decreasing with increase in undercooling which in turn suggest the Cu get trapped in the primary dendritic phase. The concentration of Co rich minor phase is shown in Figure 4c which confirms that the composition was nearly uniform at different levels of undercooling. The XRD plot shown in Figure 4d confirms the FCC primary phase was present in all levels of undercooling. From XRD analysis of samples with undercooling 54 K and 100 K it is observed that with the increase in undercooling the material get textured.

4.4 Growth velocity variation with respect to undercooling

The growth velocity variation by tracking the solid-liquid interface is shown in Figure 5. The velocity increased with increase in undercooling. The lower under-

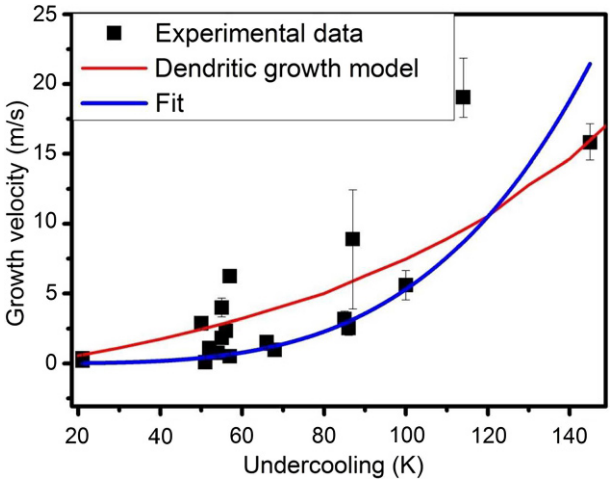

Fig. 5. Growth velocity variation with respect to undercooling where the black square shows the experimental values, continuous line shows the non linear fit.

cooling regime was governed by the diffusion controlled and the higher undercooling regime was governed by collision or thermal controlled. The undercooling trend was comparable to some reported alloys which confirm that the growth velocity was not sluggish at the higher undercooling regime for the studied equiatomic alloy [20,29]. The growth velocity was increasing nonlinearly with undercooling can be fit using non-linear equation as shown in Figure 5. The expression for the nonlinear fit is as follows

$$\text{Growth velocity}\,(V) = 1.544 \times 10^{-7}\,(\Delta T)^{3.767}\,.$$

The bulk undercooling obtained has a contribution from solutal, curvature, thermal and kinetic undercooling. Dendritic growth models are established to predict the growth velocity, undercooling contribution and dendritic tip radius with respect to undercooling obtained. Different models are established in literature based on marginal stability criteria like LKT model [30], BCT model [31] and based on microscopic solvability criteria which predict more realistic values [32]. The models' predictability depends on the parameters optimised as well as thermodynamic, kinetic and diffusion data available for the system. The dendritic growth model with a pseudo-binary approach used for the current system is explained below [31,33]

$$\text{Bulk undercooling, } \Delta T = \Delta T_t + \Delta T_s + \Delta T_k + \Delta T_r \tag{1}$$

each term can be expanded as

$$\text{Thermal undercooling}\,\Delta T_t = \Delta T_{\text{hyp}}\text{Iv}\,(P_t) \tag{2}$$

where ΔT_{hyp} is hypercooling= $(\Delta H/C_i)$ in which the latent heat of fusion (ΔH) and heat capacity of liquid (C_i) was found from Thermo-Calc® data, $\text{Iv}(P_t)$ is the Ivantsov function where P_t is the thermal Peclet number

$$\text{Solutal undercooling}\,\Delta T_s = mC_0\left\{1 - \left\{\frac{\frac{m'}{m}}{1-(1-k)\,\text{Iv}\,(Pc)}\right\}\right\} \tag{3}$$

where m = slope of liquidus, found from the Thermo-Calc® data and m' = slope of kinetic liquidus can be found from the equilibrium partition coefficient and k is the

Table 2. Values of parameters used in the dendritic growth model calculations.

Kinetic coefficient (K)	1011	Present work
Super cooling (K)	226.6	From Thermo Calc
Thermal diffusivity (m^2/s)	1.7×10^{-5}	Present work
Gibbs–Thomson coefficient (Km)	2.825×10^{-11}	Present work
Velocity sound (m/s)	2000	Present work
Partition coefficient	0.322	From experiment
Composition (at%)	33.333	From experiment
m_0 (liquidus slope) (K/at%)	−4.178	From Thermo Calc
Diffusion velocity (m/s)	5	Present work
Interface diffusion velocity (m/s)	5	Present work
Solute diffusivity (m/s)	1.75×10^{-9}	Present work

velocity dependent partition coefficient and Pc is the Solutal Peclet Number

$$\text{Curvature undercooling } \Delta T_r = 2\Gamma/r \tag{4}$$

where Γ is Gibbs–Thomson coefficient and r is the dendritic tip radii

$$\text{Modified kinetic undercooling } \Delta T_k = \mu(v/v_c)^n \tag{5}$$

where μ kinetic coefficient is given by $(RT_L^2/\Delta H)$, R is universal gas constant, and v_c is the maximum growth rate at the infinite driving force.

Apart from equation (1) the stability criteria required to solve the equations to get dendritic growth velocity and tip radius was explained elsewhere [30,33–35].

Here the kinetic undercooling term was modified with a power n ($n = 0.57$) which allows fitting the experimental data of equiatomic system with the predicted growth velocity data. The value of n and the input variables for the current system is listed in Table 2. From Figure 5 we can conclude that the prediction from the dendritic growth model can be used for multicomponent alloys also.

4.5 Phase-field simulation of undercooled sample

The phase field model uses a diffuse interface approach with an order parameter Φ for different phases. In the current simulation of solidification of dendritic phase, the order parameter Φ takes a value 1 for solid phase and 0 for the liquid phase and Micress® uses a value of −1 for the interface. The simulated phase field plots shown in Figure 6 confirms the increase in growth velocity with respect to the increase in undercooling. The phase fields are plotted by keeping all parameters constant and varying the undercooling. It is found that with the same time period the higher undercooling will result in the formation of secondary arms and also the dendritic growth velocity qualitatively high with an increase in undercooling which in turn matches with the trend obtained from experiments. The segregation profile of Cu and Co plotted shows the enrichment of Cu at interdendritic region and enrichment of Co at the dendritic region. Figure 7 shows the segregation profile with multiple dendrites with an undercooling of 21 K. The simulated profile shows Cu is enriching in the interdendritic region and the Co having variation in concentration within the dendrite. The Co concentration near the dendrite tip shows enrichment more than the centre of dendrite may due to the Cu segregation in the interdendritic region. This increase in Co concentration at dendritic tip observed dendrites at the centre which is surrounded by other dendrites and also strong Cu rich region around the

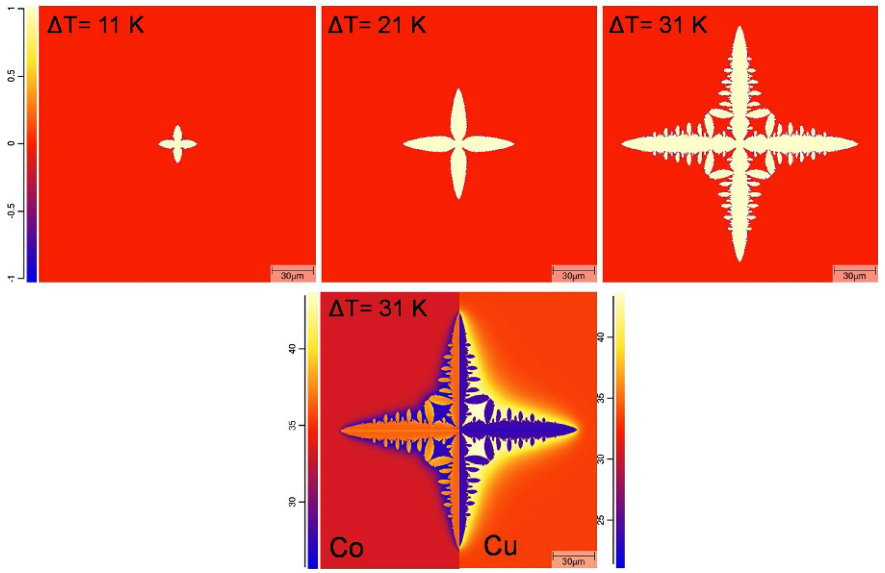

Fig. 6. Phase field plot at different levels of undercooling and segregation map shows Cu get enriched in the interdendritic region and Co get enriched in the dendritic region.

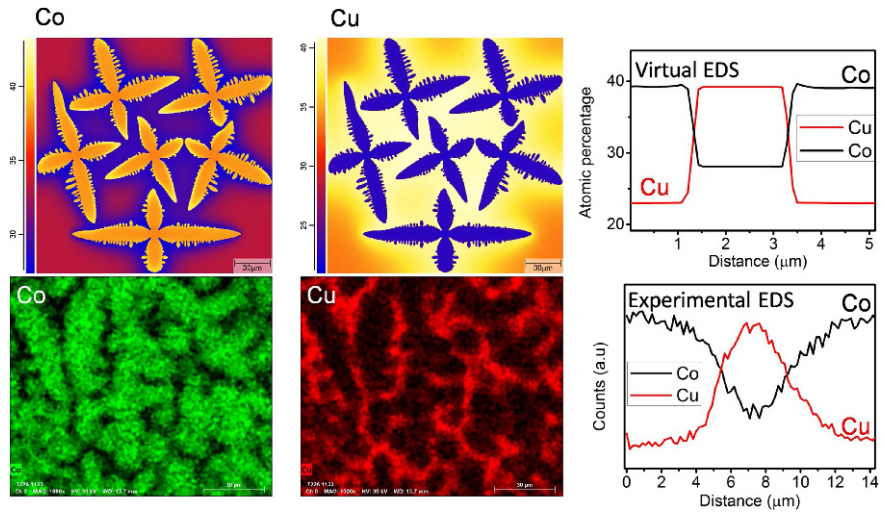

Fig. 7. Comparison of simulated segregation profile with multiple dendrite and EDS mapping of undercooled sample ($\Delta T = 21\,\mathrm{K}$) and comparison of virtual and experimental line EDS profile.

dendrite. The experimental EDS maps show the segregation profile was comparable to the simulated microstructure. The virtual line EDS and experimental line EDS confirm the applicability of simulation to use real-time microstructure prediction.

The micro-hardness measurements were taken for the current studied alloy. The as cast condition shows an average micro-hardness value of $169 \pm 10\,\mathrm{HV}$ and it was increased to $183 \pm 12\,\mathrm{HV}$ at an undercooling of $145\,\mathrm{K}$. The average value shows an increasing trend in hardness due to undercooling may due to multiple effects like solute trapping leads to solid solution strengthening and refinement of microstructure.

The improvement in hardness with undercooling was reported in Fe based commercial alloys [36].

5 Conclusion

Undercooling studies on equiatomic CoCuNi system was carried out using melt fluxing technique and achieved a maximum undercooling of $0.11T_L$. The microstructure variation was established and correlated with the undercooling obtained. The growth velocity shows a non-linear increase with undercooling and correlated with the established dendritic growth model with modification in the kinetic term. The EDS results suggest that solute trapping occurs on the sample and with respect to undercooling the solute concentration was changed. The segregation profile was predicted by using phase field simulation and is matching with the experimental profiles. The hardness variation was correlated with the undercooling.

References

1. D.B. Miracle, O.N. Senkov, Acta Mater. **122**, 448 (2017)
2. O.N. Senkov, J.D. Miller, D.B. Miracle, C. Woodward, Nat. Commun. **6**, 6529 (2015)
3. S. Praveen, J.W. Bae, P. Asghari-Rad, J.M. Park, H.S. Kim, Mater. Sci. Eng. A **735**, 394 (2018)
4. X.W. Liu, G. Laplanche, A. Kostka, S.G. Fries, J. Pfetzing-Micklich, G. Liu, E.P. George, J. Alloys Compd. **775**, 1068 (2019)
5. G. Dan Sathiaraj, W. Skrotzki, A. Pukenas, R. Schaarschuch, R. Jose Immanuel, S.K. Panigrahi, J. Arout Chelvane, S.S. Satheesh Kumar, Intermetallics **101**, 87 (2018)
6. Z. Wu, W. Guo, K. Jin, J.D. Poplawsky, Y. Gao, H. Bei, J. Mater. Res. **33**, 3301 (2018)
7. B. Gludovatz, A. Hohenwarter, D. Catoor, E.H. Chang, E.P. George, R.O. Ritchie, Science. **345**, 1153 (2014)
8. B.S. Murty, J.W. Yeh, S. Ranganathan, P.P. Bhattacharjee, *High-entropy alloys*, 2nd edn. (Elsevier, 2019)
9. S. Chen, Y. Tong, P.K. Liaw, Entropy **20**, 937 (2018)
10. S. Gorsse, C. Hutchinson, M. Gouné, R. Banerjee, Sci. Technol. Adv. Mater. **18**, 584 (2017)
11. A. Munitz, M.J. Kaufman, R. Abbaschian, Intermetallics **86**, 59 (2017)
12. Z. An, H. Jia, Y. Wu, P.D. Rack, A.D. Patchen, Y. Liu, Y. Ren, N. Li, P.K. Liaw, Mater. Res. Lett. **3**, 203 (2015)
13. A. Verma, P. Tarate, A.C. Abhyankar, M.R. Mohape, D.S. Gowtam, V.P. Deshmukh, T. Shanmugasundaram, Scr. Mater. **161**, 28 (2019)
14. W.L. Wang, L. Hu, S.B. Luo, L.J. Meng, D.L. Geng, B. Wei, Intermetallics **77**, 41 (2016)
15. M. Beyramali Kivy, M. Asle Zaeem, S. Lekakh, Mater. Des. **127**, 224 (2017)
16. R. Sonkusare, A. Swain, M.R. Rahul, S. Samal, N.P. Gurao, K. Biswas, S.S. Singh, N. Nayan, Mater. Sci. Eng. A. **759**, 415 (2019)
17. M.R. Rahul, S. Samal, G. Phanikumar, J. Mater. Res. **34**, 700 (2019)
18. N. Liu, P.H. Wu, P.J. Zhou, Z. Peng, X.J. Wang, Y.P. Lu, Intermetallics **72**, 44 (2016)
19. C.D. Cao, D.M. Herlach, M. Kolbe, G.P. Görler, B. Wei, Scr. Mater. **48**, 5 (2003)
20. P.R. Algoso, W.H. Hofmeister, R.J. Bayuzick, Acta Mater. **51**, 4307 (2003)
21. N.G. Jones, R. Izzo, P.M. Mignanelli, K.A. Christofidou, H.J. Stone, Intermetallics **71**, 43 (2016)
22. J.F. Li, Y.H. Zhou, G.C. Yang, Mater. Sci. Eng. A **277**, 161 (2000)
23. D.Y. Zang, H.P. Wang, F.P. Dai, D. Langevin, B. Wei, Appl. Phys. A **102**, 141 (2011)
24. J. Eiken, B. Böttger, I. Steinbach, Phys. Rev. E **73**, 066122 (2006)
25. B. Böttger, J. Eiken, M. Apel, Comput. Mater. Sci. **108**, 283 (2015)

26. P.K. Galenko, S. Reutzel, D.M. Herlach, S.G. Fries, I. Steinbach, M. Apel, Acta Mater. **57**, 6166 (2009)
27. A. Takeuchi, A. Inoue, Mater. Trans. **46**, 2817 (2005)
28. T. Zhang, F. Liu, H.F. Wang, G.C. Yang, Scr. Mater. **63**, 43 (2010)
29. K. Eckler, D.M. Herlach, Mater. Sci. Eng. **178**, 159 (1994)
30. J. Lipton, W. Kurz, R. Trivedi, Acta Mater. **35**, 957 (1987)
31. W.J. Boettinger, S.R. Coriell, R. Trivedi, Rapid Solidif. Process. Princ. Technol. **4**, 13 (1988)
32. D.V. Alexandrov, D.A. Pinigin, Tech. Phys. **58**, 309 (2013)
33. G. Phanikumar, K. Biswas, O. Funke, D. Holland-Moritz, D.M. Herlach, K. Chattopadhyay, Acta Mater. **53**, 3591 (2005)
34. D. Mohan, G. Phanikumar, Philos. Trans. R. Soc. A **377**, 20180208 (2019)
35. W. Löser, D.M. Herlach, Metall. Trans. A **23**, 1585 (1992)
36. Y. Ruan, S.Y. Chang, M. Dao, Cryst. Growth Des. **15**, 5661 (2015)